Electronic Supplementary Material (ESI) for Soft Matter.

Supplementary Information

Buckling of paramagnetic chains in soft gels

Shilin Huang,[a] Giorgio Pessot,[b] Peet Cremer,[b] Rudolf Weeber,[c]
Christian Holm,[c] Johannes Nowak,[d] Stefan Odenbach,[d]
Andreas M. Menzel,[b] Günter K. Auernhammer[a]

[a] Max Planck Institute for Polymer Research, Ackermannweg 10, 55128 Mainz, Germany.
[b] Institut für Theoretische Physik II: Weiche Materie, Heinrich-Heine-Universität Düsseldorf, D-40225 Düsseldorf, Germany.
[c] Institute for Computational Physics, Universität Stuttgart, 70569 Stuttgart Germany.
[d] Chair of Magnetofluiddynamics, Measuring and Automation Technology, Institute of Fluid Mechanics, Technische Universität Dresden, 01069 Dresden, Germany.

1 Supplementary movies

Movie S1 Typical 3D morphology of paramagnetic chains in a soft gel in the absence of a magnetic field. The elastic modulus of the gel is 0.78 ± 0.22 Pa and the scale bar is 300 μm.

Movie S2 Typical 3D morphology of paramagnetic chains in a soft gel under a perpendicular magnetic field ($B = 216.4 \pm 1.1$ mT). The elastic modulus of the gel is 0.78 ± 0.22 Pa and the scale bar is 300 μm.

2 Supplementary information for experiments

2.1 Paramagnetic particles

According to the manufacturer (microParticles GmbH), the paramagnetic particles were fabricated based on porous polystyrene particles. Within the pores of the polystyrene particles, nanoparticulate iron oxide was distributed, rendering the particles superparamagnetic. To prevent iron oxide leaching, the paramagnetic particles were covered with thin polymer layers which also held the fluorophores. The diameter of the paramagnetic particles from the scanning electron microscopy (SEM) images (see Fig. S1a) is 1.4 ± 0.2 μm. We also measured the length of linear particle chains in polydimethylsiloxane using laser scanning confocal microscopy (LSCM). Dividing the length of the chains by the number of particles in the chains we got a diameter of 1.48 ± 0.13 μm (average for 20 chains). We used the latter value for calibration and calculation in this paper.

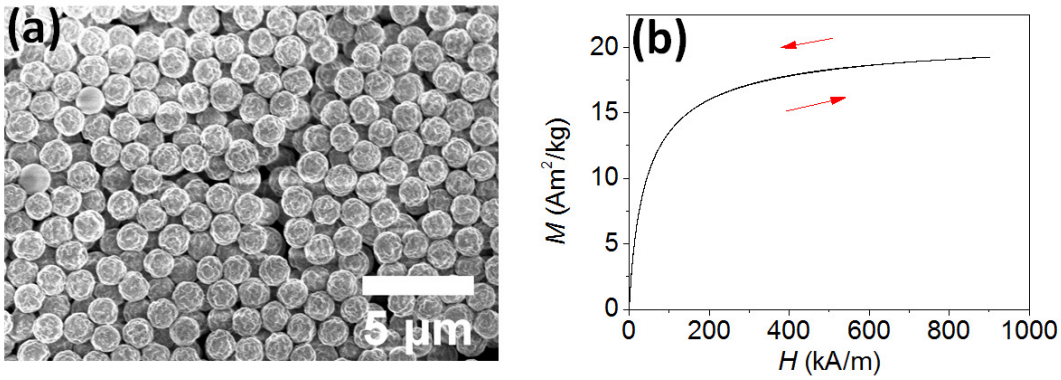

Figure S1 (a) Scanning electron microscopy (SEM) image of the paramagnetic particles. The scale bar is 5 μm. (b) Magnetization curve of the paramagnetic particles. The magnetic field H was increased from 0 kA/m to 900 kA/m and then decreased to 0 kA/m, and the magnetization M showed no hysteresis, as indicated by the red arrows.

The magnetization curve of the paramagnetic particles was measured by a vibrating sample magnetometer (VSM, Lake Shore 7407). The magnetization of the particles showed no hysteresis when the external magnetic field was increased and decreased, demonstrating the superparamagnetic property (Fig. S1b).

2.2 Calibrating the magnetic properties of the paramagnetic particles

A spherical colloidal particle moving in a viscous fluid with a relative velocity $\mathbf{v}$ is subject to a frictional force (Stokes' drag)

$$\mathbf{F}_d = -6\pi\eta R\mathbf{v}, \tag{S1}$$

where R is the radius of the particle and η is the dynamic viscosity of the fluid.

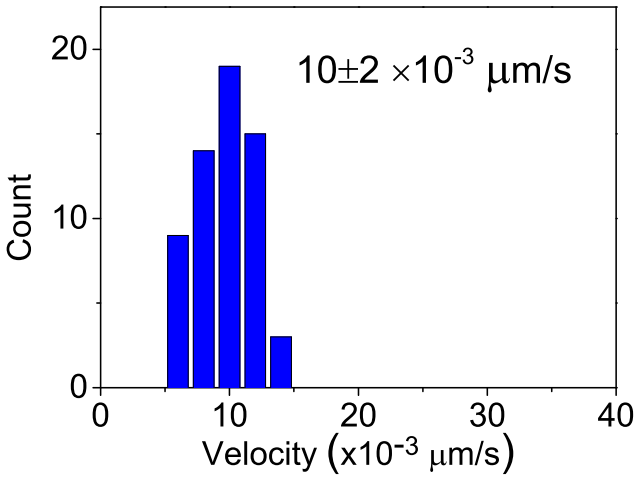

Figure S2 Histogram of velocity of paramagnetic particles moving in a viscous liquid. The viscosity of the liquid is 0.61 ± 0.02 Pa s. The magnetic field strength is 32.7 ± 0.2 mT and the magnetic gradient is $3.63 \pm 0.02 \times 10^{-5}$ mT/μm. Using a density of 1.7 g/cm^3, the movement of the particles, the magnetic gradient, and the magnetization curve can be correlated.[S1,S2]

Under a magnetic field $\mathbf{B}$, the magnetic particles move along the magnetic field gradient. The magnetic force $\mathbf{F}_m$ acting on a paramagnetic particle is[S1,S2]

$$\mathbf{F}_m = \mathbf{m} \cdot \nabla \mathbf{B}, \tag{S2}$$

where $\mathbf{m}$ is the induced magnetic dipole moment of the paramagnetic particle. In the steady state, the magnetic force is balanced by Stokes' drag, thus

$$6\pi\eta R\mathbf{v} = \mathbf{m} \cdot \nabla \mathbf{B}. \tag{S3}$$

From experiments, the left-hand side of Eq. (S3) and $\nabla \mathbf{B}$ can be measured directly. We dispersed the paramagnetic particles into a viscous liquid with a viscosity of 0.61 ± 0.02 Pa s. The dispersion was added into a sample cell with a thickness of 160 μm. Then the sample cell was carefully sealed in order to avoid drift due to large-scale flow of the liquid. We used a magnetic field of 32.7 ± 0.2 mT with a gradient of $3.63 \pm 0.02 \times 10^{-5}$ mT/μm to induce flow of the paramagnetic particles. The magnetic field was measured by a Lake Shore Model 425 Gaussmeter with a transverse probe. The movement of the particles (far from the walls of the sample cell) was recorded using LSCM. The magnitude of the magnetic moment m can be calculated via $m = 4\pi R^3 \rho M/3$, where M can be obtained from the magnetization curve (Fig. S1b) and ρ is the density of the paramagnetic particles. Using $\rho = 1.7$ g/cm^3, we find that Eq. (S3) is satisfied. This density value is in agreement with the one provided by the manufacturer (1.5–2 g/cm^3).

In our study the paramagnetic particles are not ideally monodispersed and the induced magnetic moment is not ideally identical for every particle. For example, the velocity of the paramagnetic particles moving in a viscous liquid under a magnetic gradient has a distribution with $\sim 20\%$ deviation (Fig. S2). According to Eq. (S3), the magnetic moment of the particles should have a similar distribution. For simplification, we do not consider this distribution in the modeling and simulation.

2.3 Determining the elastic modulus of the soft gels

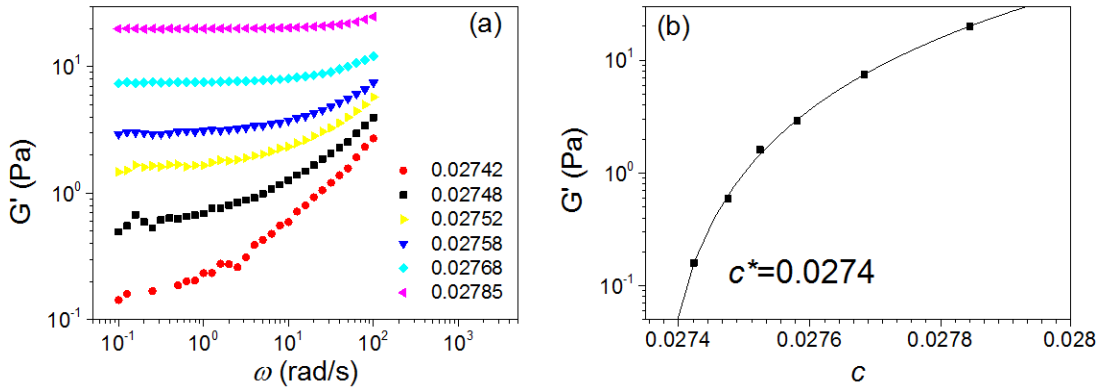

Figure S3 (a) Shear elastic modulus (G') of the gels as a function of angular frequency. The gels were fabricated with different concentrations (c) of the prepolymer mixture as indicated for the different sets of data points. (b) The low-frequency G' of the gels plotted as a function of c. The solid curve is the best fit of Eq. (S4) to the experimental data.

The rheological experiments were performed in a strain-controlled rheometer (ARES-LS, Rheometric Scientific Inc., Piscataway, NJ, USA) equipped with a Couette cell at room temperature. The elastic modulus (G') shows a plateau at low frequencies for the soft gels (Fig. S3a), reflecting the formation of a percolating network. The plateau modulus increases with increasing concentration of the prepolymer mixture (c) following a power law[S3]

$$G' = G'_0(c - c^\star)^t, \tag{S4}$$

where G'_0 is a prefactor, t is the critical exponent, and $c^\star$ is the percolation concentration. From this power law it is evident that the elastic modulus of the soft gels becomes very sensitive to the concentration of the prepolymer mixture when the concentration of the prepolymer mixture is close to $c^\star$.

As a result, we cannot directly use the elastic modulus obtained from macroscopic rheological measurements to characterize our soft gels in the sample cells ($\sim$160 μm thick), because a little change of the concentration of the prepolymer mixture during preparation of the gels can lead to a significant difference of the elastic modulus. In experiment, the concentration of the prepolymer mixture in the sample cells is difficult to control precisely, because the concentration can change slightly if some prepolymer molecules are adsorbed to the walls of the cell, to the pipette tips, or to the paramagnetic particles.

In order to solve this problem, we measured the elastic modulus of the soft gels directly in the sample cells (containing the paramagnetic chains) by passive microrheology (i.e., particle tracking). About 15 single particles were used as the mechanical probes, and a fast camera (Photron, FASTCAM SA1) and a microscope (Leica DMI6000B) were used to detect the thermal fluctuations of the particles.[S4,S5] Fig. S4a shows the mean-square displacement (MSD) of the particles in the gels as a function of lag time. At long lag times the MSD levels off, indicating that the particles are confined in a network. The moduli of the gels can be calculated from the MSD of the particles based on the generalized

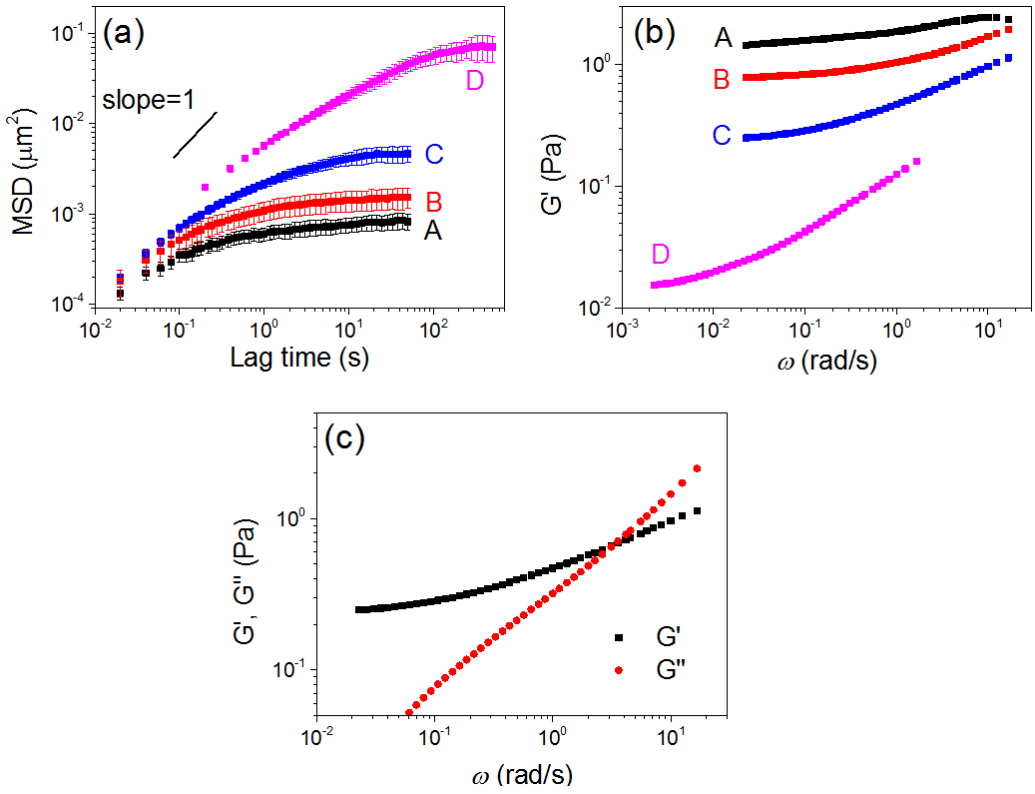

Figure S4 Probing the viscoelastic properties of the gels in the sample cells (containing the paramagnetic chains). (a) Mean-square displacement (MSD) of the particles in the gels as a function of lag time. The concentrations of the prepolymer mixture for the four samples A–D are 2.78 wt%, 2.77 wt%, 2.76 wt%, and 2.76 wt%, respectively. The slight changes of concentration can lead to significant differences in the MSD, because the concentration used here is close to the percolation threshold ($c^\star = 2.74\%$, see Fig. S3b).[S3] It is the method of passive microrheology that makes it possible to measure the viscoelastic properties of the soft gels (containing the paramagnetic chains) directly within the sample cells. (b) Elastic modulus (G') calculated from the MSD. (c) Elastic modulus (G') and loss modulus (G'') plotted as functions of angular frequency (ω) for sample C. At low frequencies, the elastic character dominates.

Stokes-Einstein relation (GSER)[S4,S6]

$$G^*(\omega) = \frac{k_B T}{\pi R (i\omega) \mathscr{F}_u\{MSD(t)\}}, \tag{S5}$$

where $G^*(\omega)$ is the complex shear modulus and $\mathscr{F}_u\{MSD(t)\}$ is the unilateral Fourier transform ($\mathscr{F}\{f(t)\} = \int_0^\infty e^{-i\omega\tau} f(\tau)\, d\tau$). Using the algorithm from Crocker and Weeks,[S4,S5] we calculated the shear moduli (Fig. S4b). Fig. S4c shows that at low frequencies (corresponding to long time scales) the gel is mainly elastic. In the main article we use the elastic modulus of the gels obtained from passive microrheology to characterize the gels.

2.4 Magnetic field of the Halbach magnetic array

We used permanent magnets to provide a homogeneous magnetic field.[S7] The NdFeB permanent magnets were purchased from AR.ON GmbH. According to the manufacturer they have a remanence of 1.32 T. The magnets were arranged as shown in Fig. 1a. The magnets had dimensions of $8 \times 8 \times 15$ mm^3 and $14 \times 14 \times 15$ mm^3 for the inner and outer rings, respectively. The magnetic field at the center of this magnetic array was homogeneous (Fig. S5). This magnetic array was built around the objective of our home-built LSCM and it could be rotated by a motor. We put the samples in the middle of this array and used LSCM to observe the samples under the magnetic field. The typical observation area was in the central 2 mm^2, where the homogeneity of the magnetic field was $\sim 2\,000$ ppm (Fig. S5b).

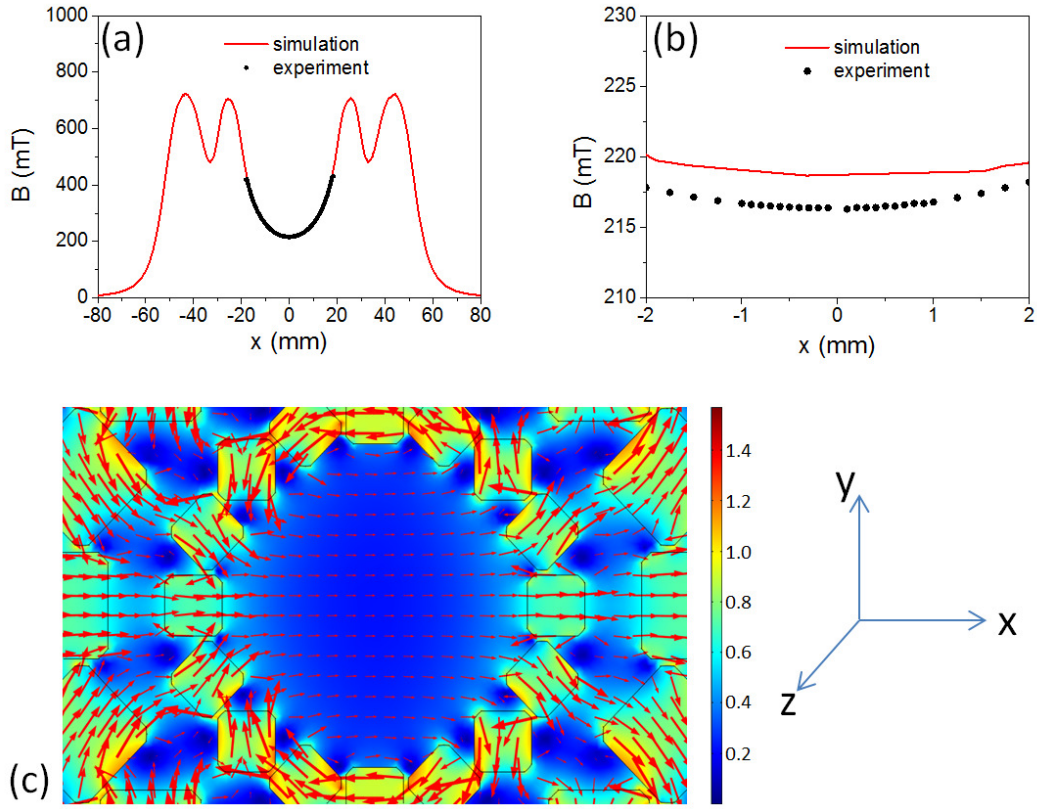

Figure S5 Comparison of measured and simulated magnetic flux density in the Halbach magnetic array. The arrangement of the 32 permanent magnets is shown in Fig. 1a. (a) Magnitude B of the magnetic flux density along the x-axis. The red solid curve shows simulation results using Comsol software. The solid black points are experimental data (measured by a Lake Shore Model 425 Gaussmeter with a transverse probe). The data for x around 0 are shown in (b). The homogeneity in the central 2 mm^2 is $\sim 2\,000$ ppm. (c) Simulated magnetic field in the magnetic array. The magnetic flux density is shown by color map and the direction of the magnetic field is shown by red arrows.

The magnetic field of this magnetic array was simulated in Comsol Multiphysics (http://www.comsol.com). The parameters for the simulation were the same as in the experiments, such as the positions, the dimensions, and the remanence (1.32 T) of the magnets. The permanent magnets were modeled using Ampère's law. The influence of

the housing (made of Aluminum) of the magnets was not considered. A detailed description of the simulation can be found in the model library of Comsol Multiphysics, "Static Field Modeling of a Halbach Rotor".

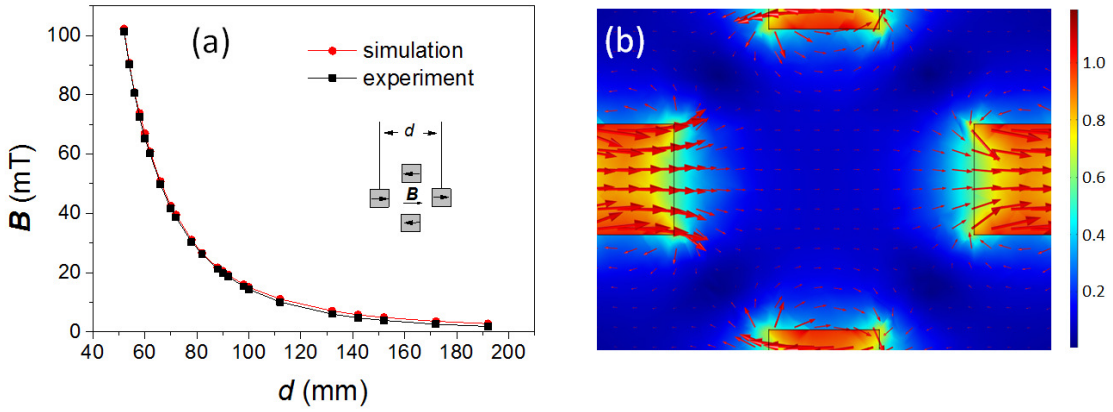

Figure S6 Magnetic field of the four-magnet Halbach array. (a) By changing the separation between the 4 magnets, the magnetic flux density at the center of the magnetic array can be changed. The red circle points are obtained from simulation using Comsol software, and the black square points are measured by a Lake Shore Model 425 Gaussmeter with a transverse probe. The homogeneity in the central 2 mm^2 is ~ 4000 ppm. (b) Simulated magnetic field in the four-magnet array. The magnetic flux density is shown by color map and the direction of the magnetic field is shown by red arrows.

In some experiments we needed to change the magnetic field strength. This was realized by using a four-magnet Halbach array (Fig. S6, the magnets had dimensions of $14 \times 14 \times 15$ mm^3). By changing the distance between the magnets, the magnetic flux density in the center of this array could be changed from 0 mT to 101 mT. The homogeneity of this array in the central 2 mm^2 was ~ 4000 ppm.

2.5 Bending rigidity of the paramagnetic particle chains

Here we provide experimental evidence that the paramagnetic particle chains already by themselves (i.e. without the embedding polymer matrix) feature a bending rigidity. For this purpose, instead of preparing a percolating polymer network (gel), we prepared a sol. We decreased the concentration of the prepolymer mixture to $c^\star/2$ ($c^\star$ is the critical concentration at which a percolating network can be formed, see Fig. S3b). The prepolymer mixture reacted and formed a sol after the catalyst was added. During the reaction a magnetic field of 100.8 mT was applied, thus the magnetic particles in the sol aligned into chains. If the particles had not been connected by the polymer, the linear particle chains would not have survived after the magnetic field was removed because of thermal agitation. However, we found that the linear particle chains were stable in the sol even for several days (Fig. S7a). Once more applying a magnetic field (18.7 mT) most of the permanent paramagnetic chains in the sol aligned along the magnetic field direction (Fig. S7b). However, some of the chains bent and showed hairpin or "S"-shape morphologies (marked by the red arrows in Fig. S7b), indicating that the chains had a bending rigidity.[S8]

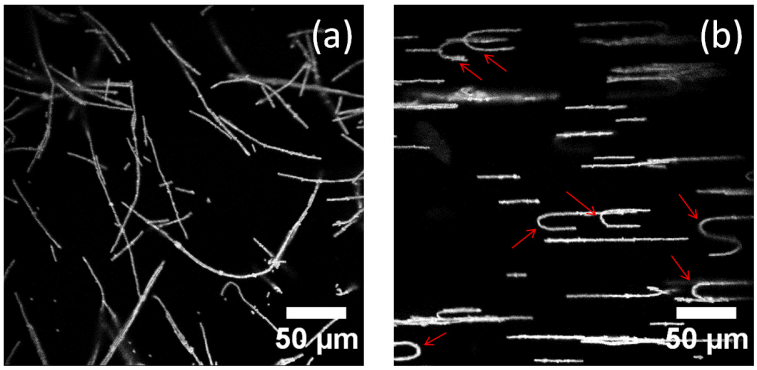

Figure S7 Typical chain morphologies in the sol (a) in the absence of a magnetic field and (b) under a magnetic field. The magnetic field of 18.7 mT was applied horizontally. Under the magnetic field most of the paramagnetic chains aligned along the magnetic field direction. Some of the chains bent and showed hairpin or "S"-shape morphologies (marked by the red arrows), indicating that they have a bending rigidity.[S8] The scale bars are 50 μm.

We conjecture that some prepolymer molecules in the solution were adsorbed onto the surfaces of the paramagnetic particles. When the prepolymer cross-linked, a polymer layer on the surfaces of the particles was formed and connected the particles. This polymer layer contributed to the bending rigidity. Only when the concentration of the prepolymer mixture is higher than $c^\star$, a gel can be formed in the bulk. Apparently, already below this concentration, a connecting polymer layer can be formed on the surfaces of the paramagnetic particles. This suggests that a thin layer of polymer with a higher modulus compared to the bulk should be considered to understand the buckling behavior of the paramagnetic chains in the soft gels.

2.6 Buckling of magnetic particles in a "stiff" gel

In the main article, very soft gels (<1.5 Pa) were used as a matrix. If a stiffer gel was used, the paramagnetic particle chains could not deform the gel significantly under the magnetic field of 216 mT (maximum field in our set-up). Here we used carbonyl iron (CI, CC grade, BASF, Germany, d50 value=3.8-5.3 μm) as magnetic particles in order to increase the magnetic force between the magnetic particles. First, the saturation of magnetization of CI (~ 250 Am^2/kg) is significantly larger than that of our otherwise used paramagnetic particles (~ 20 Am^2/kg); second, the density of CI ($\sim 8\times10^3$ kg/m^3) is higher than that of our paramagnetic particles ($\sim 1.7\times10^3$ kg/m^3); last, the size of CI is about 3 times larger. According to $m = 4\pi R^3\rho M/3$ (see Section 2.2), the magnetic moment can be 10^3 times larger compared to our paramagnetic case in the main article. As a result, even in a relatively "stiff" gel, the CI magnetic chains can deform the gel significantly. As shown in Fig. S8, in the gel with an elastic modulus of 170 Pa, the CI chains can buckle when a magnetic field of 100.8 mT is applied.

However, promoted by the polydispersity of the CI particles, the CI chains are not as smooth as the chains formed by the monodisperse paramagnetic particles (see Figs. 1 and 2 in the main article for comparison). In addition, we also observed fractures in some CI chains (Fig. S8c) probably due to the polydispersity of the particles. However, the chains

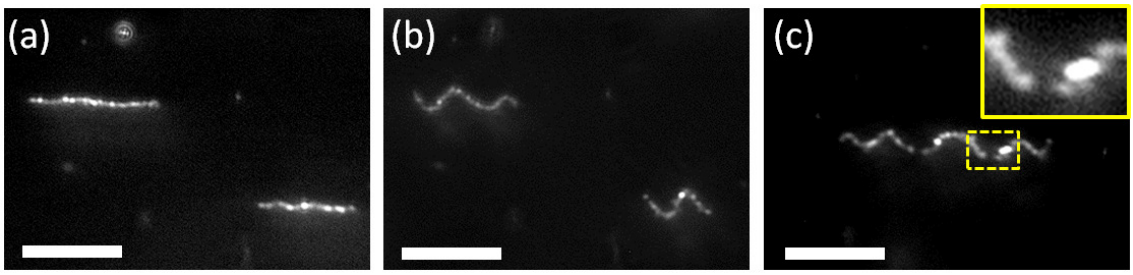

Figure S8 Magnetic chains formed by carbonyl iron particles in a gel with an elastic modulus of 170 Pa. (a) Without magnetic field, (b, c) under a magnetic field of 100.8 mT along the vertical direction. The inset in (c) shows an enlarged image of the fracture of the magnetic chain. The scale bars are 50 μm. These images were obtained using a 10$\times$ objective (NA=0.28, M Plan Apo) which collected the reflection light from the carbonyl iron particles.

do not break up into structures as shown in Fig. 9 of the main article (lower image), suggesting that there is still a relatively stiff polymer layer around the CI particles.

3 Supplementary information concerning the modeling

3.1 Magnetic interactions within the chain

In the following, we derive Eqs. (1) and (2) of the main article. We start from two neighboring particles on the chain. According to the assumptions made in the main article, each of them carries a magnetic moment $\mathbf{m}$ oriented in y-direction. They interact via the dipole-dipole magnetic interaction given by

$$V_{dd} = \frac{\mu_0}{4\pi}\left[\frac{\mathbf{m}\cdot\mathbf{m}}{r^3} - \frac{3\,(\mathbf{m}\cdot\mathbf{r})\,(\mathbf{m}\cdot\mathbf{r})}{r^5}\right], \tag{S6}$$

where $\mathbf{r}$ is the vector joining the centers of the particles, $r = |\mathbf{r}|$, and μ_0 is the vacuum magnetic permeability. Since the particles on the chain are experimentally observed to remain in contact, we have $r = d$, with d the particle diameter. Furthermore, we ignore the first term in the square brackets because it is constant under the given assumptions. Indicating by α the angle between $\mathbf{r}$ and $\mathbf{m}$, we obtain

$$V_{dd} \sim -\frac{3\mu_0 m^2}{4\pi d^3}\cos^2\alpha. \tag{S7}$$

Since $\mathbf{m}$ is oriented in the y-direction, $\psi = \pi/2 - \alpha$ is the angle between $\mathbf{r}$ and the x-axis. Skipping another constant term resulting from $\cos^2\alpha = 1 - \sin^2\alpha$, the non-constant part of the dipole-dipole interaction can thus be rewritten as

$$V_{dd} \sim \varepsilon_m \sin^2(\psi - \pi/2), \quad \text{with } \varepsilon_m = \frac{3\mu_0 m^2}{4\pi d^3}. \tag{S8}$$

For an undeformed infinite straight chain oriented along the x-axis in the above set-up, the resulting expression for the total dipolar magnetic interaction energy per particle along the whole chain then reads

$$V_{dd}^{chain} \sim \varepsilon_m \sum_{n=1}^{\infty} \frac{1}{n^3} = \varepsilon_m \zeta(3), \tag{S9}$$

where ζ is the Riemann Zeta function and $\zeta(3) \simeq 1.202$. Here, ε_m sets the scale of the nearest-neighbor dipolar interaction. In our minimal model the correction described by the factor $\zeta(3) \simeq 1.202$ due to higher-order neighbors is negligible. Since the contour lines of the magnetic chains preserve a smooth shape under the observed deformations, without any kinks, and as the chains do not fold back onto themselves, we thus confine ourselves to nearest-neighbor interactions.

For a large number of particles, the quantity ε_m sets the magnetic interaction energy per particle. Moreover, the total magnetic interaction energy scales approximately linearly with the number of particles and chain length.

We now switch to a continuum picture by specifying the line energy density along the magnetic chain. In our coordinate system, the angle ψ that the connecting vector $\mathbf{r}$ between two neighboring particles forms with the x-axis is locally given by $\psi \sim$

arctan $[y'(x)]$, where $y'(x) = dy/dx$. To obtain the resulting magnetic energy of the whole magnetic chain, we need to integrate the energy line density along the contour line. For simplicity, we transform this line integral to an integration along the x-axis. If we parameterize the contour line by the parameter s, the line element ds along the chain can be expressed as $ds = \sqrt{1+y'(x)^2}\,dx$. Therefore, the magnetic energy becomes

$$\begin{aligned} E_{magn}[y] &= W \int_{x_1}^{x_2} \sin^2\left\{\arctan\left[y'(x)\right] - \frac{\pi}{2}\right\} \sqrt{1+y'(x)^2}\,dx \\ &= W \int_{x_1}^{x_2} \frac{1}{\sqrt{1+y'(x)^2}}\,dx, \end{aligned} \tag{S10}$$

where

$$W = \frac{\varepsilon_m}{d} = \frac{3\mu_0 m^2}{4\pi d^4} \tag{S11}$$

is the magnetic energy per unit length and x_1, x_2 are the x-coordinates of the end points of the chain.

3.2 Elastic bending energy

Next, we briefly sketch the derivation of the elastic bending energy in Eq. (3) of the main article. For this purpose, we consider a parameterization $\mathbf{R}(s)$ of the contour line of the magnetic chain, where the positions $\mathbf{R}$ mark the points on the contour line and $s \in [s_1, s_2]$ with s_1 and s_2 labeling the end points of the chain. On this basis, the elastic bending energy is defined as[S9]

$$E_{bend} = C_b \int_{s_1}^{s_2} \left| \frac{d^2\mathbf{R}(s)}{ds^2} \right|^2 ds. \tag{S12}$$

Using the parameterization $\mathbf{R} = (x, y(x))$ and $ds = \sqrt{1+y'(x)^2}\,dx$, we obtain

$$\frac{d\mathbf{R}}{ds} = \left(1+y'(x)^2\right)^{-\frac{1}{2}} \begin{pmatrix} 1 \\ y'(x) \end{pmatrix} \tag{S13}$$

and

$$\frac{d^2\mathbf{R}}{ds^2} = y''(x)\left(1+y'(x)^2\right)^{-2} \begin{pmatrix} -y'(x) \\ 1 \end{pmatrix}. \tag{S14}$$

From this last expression, we obtain Eq. (3) in the main article when we again transform the line element ds to Cartesian coordinates, $ds = \sqrt{1+y'(x)^2}\,dx$.

3.3 Elastic displacement energy

Finally, we motivate the expression for the elastic displacement energy in Eq. (4) of the main article. The part $[y(x)]^2$ corresponds to a lowest order term in the displacement $y(x)$. We weight each of the two displacement factors $y(x)$ by the amount of chain material displaced per integration interval dx, given by the length of the chain per integration

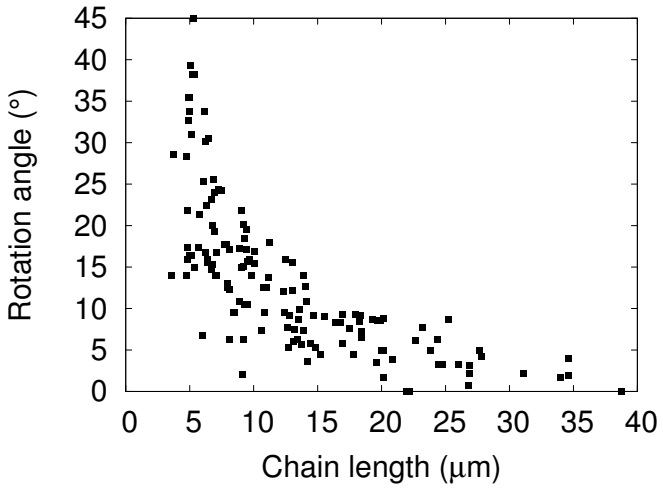

Figure S9 Experimentally observed rotation angles of magnetic chains in a gel of shear modulus $G' = 0.25$ Pa under a perpendicular magnetic field of magnitude $B = 18.7$ mT. To first approximation, a rigid rotation of straight chains occurs at small enough rotation angles. This is depicted, for instance, in Fig. 1c of the main article for small angles of the magnetic field.

interval dx, i.e. $ds/dx = \sqrt{1+y'(x)^2}$. This leads to $[y(x)]^2\left[1+y'(x)^2\right]$. In addition to that, we have another factor $\sqrt{1+y'(x)^2}$, again from transforming the line element ds of the integration to Cartesian coordinates, $ds = \sqrt{1+y'(x)^2}\,dx$. In total, we obtain the expression in Eq. (4) of the main article.

We explain in the following why the experimental observations suggest this form as a lowest order term. In particular, we note that the experimental investigations suggest the form $[y(x)]^2$ rather than one containing the first derivative $[y'(x)]^2$. For this purpose, we consider the case of straight chains ($M = 0$) undergoing small rotations in a perpendicular magnetic field. This situation can be simply parameterized by $y(x) = Sx$, where $S = \tan\psi$ and ψ as introduced above giving the rotation angle. Furthermore $E_{bend} = 0$.

For $y(x) = Sx$, E_{magn} scales linearly with the chain length L. The same would apply for an energetic contribution $\sim \int_{x_1}^{x_2}[y'(x)]^2\left[1+y'(x)^2\right]^{3/2}dx$. Therefore, the latter expression inevitably leads to a rotation angle ψ that is independent of the chain length L. However, this contradicts the experimental results. In Fig. S9 we plot the rotation angle ψ as a function of chain length L measured in a gel of shear modulus $G' = 0.25$ Pa exposed to a perpendicular magnetic field of magnitude $B = 18.7$ mT. There is a clear dependency of the rotation angle on the chain length L. The energetic expression E_{displ} in Eq. (4) of the main article for rotations of straight chains $y(x) = Sx$ scales as $E_{displ} \sim L^3$ and thus leads to disproportionally higher energetic penalties for longer chains, reflecting the experimentally observed smaller rotation angles.

3.4 Discussion of resulting chain shapes

Now that our total model energy E_{tot} is set as the sum of Eqs. (1), (3), and (4) in the main article, a standard route to determine the shape $y(x)$ of the chain would be to find the extrema of the functional $E_{tot}[y(x)]$ with respect to the function $y(x)$. For this purpose,

one calculates the functional derivative of $E_{tot}[y(x)]$ with respect to $y(x)$ and equates it with zero. The procedure is well known from the famous brachistochrone problem.[S10] There one wishes to find the shape of a curve linking two end points such that a body moving between them under gravity passes the distance in the least possible amount of time.

However, there is a fundamental difference compared to the brachistochrone problem. While calculating the functional derivative, boundary terms appear that explicitly include contributions from the end points of the chain or trajectory $y(x)$. Technically, they result from partial integration. In the brachistochrone problem, one has sufficient information to handle these boundary terms: by construction of the problem, one knows that the end points are fixed. Similarly, in other problems of infinitely extended elastic struts of periodic, periodically modulated, or localized deformations,[S11–S14] one can use the periodicity or localization to argue in favor of an evanescent influence of the boundary terms. This is very different from our present case, where the deflection encompasses the whole finite chain and in particular its end points. Unfortunately, acquiring sufficient knowledge of the associated boundary conditions would imply solving the whole complex three-dimensional nonlinear elasticity and magnetization problem, which is beyond the present scope and in fact was the reason to project to our reduced minimal model.

For completeness, however, we perform some additional variational analysis of our energy functional. We concentrate on possible solutions in the bulk that could be observed if boundary effects were absent (which is not the case for our experimentally investigated finitely-sized objects). Then, neglecting the boundary terms, the functional derivatives of Eqs. (1), (3), and (4) are calculated as follows (the dependencies of $y(x)$ and its derivatives on x is omitted for brevity on the right-hand sides):

$$\frac{\delta E_{magn}}{\delta y(x)} = W y'' \left(1-2y'^2\right)\left(1+y'^2\right)^{-\frac{5}{2}}, \tag{S15}$$

$$\frac{\delta E_{bend}}{\delta y(x)} = C_b \left[5y''^3\left(6y'^2-1\right) - 20y'y''y'''\left(1+y'^2\right) + 2y''''\left(1+y'^2\right)^2\right]\left(1+y'^2\right)^{-\frac{9}{2}}, \tag{S16}$$

and

$$\frac{\delta E_{displ}}{\delta y(x)} = C_d \left[2y - 2yy'^2 - 4yy'^4 - 3y^2y'' - 6y^2y'^2y''\right]\left(1+y'^2\right)^{-\frac{1}{2}}. \tag{S17}$$

Together, we obtain a nonlinear fourth-order differential equation for $y(x)$:

$$\begin{aligned}\frac{\delta E_{tot}}{\delta y(x)} = &\left(1+y'^2\right)^{-\frac{9}{2}}\left[-\left(1+y'^2\right)y''\left(W\left(-1+y'^2+2y'^4\right)+20C_by'y'''\right)\right.\\ &-3C_dy^2\left(1+y'^2\right)^4\left(1+2y'^2\right)y''+5C_b\left(-1+6y'^2\right)y''^3\\ &\left.-2C_dy\left(1+y'^2\right)^5\left(-1+2y'^2\right)+2C_b\left(1+y'^2\right)^2y''''\right]=0.\end{aligned} \tag{S18}$$

Eq. (S18) can in principle be solved numerically by integrating it outward from the center of the chain at $x=0$. For this purpose, a sufficient amount of "initial conditions"

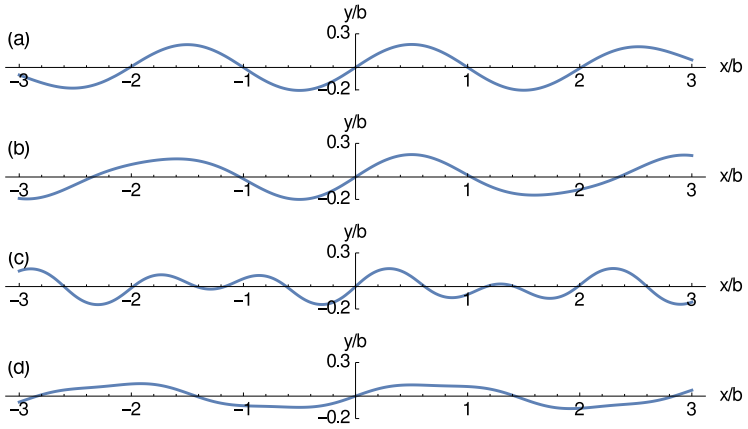

Figure S10 Numerical solutions of Eq. (S18) for different imposed input conditions. In all cases we concentrate on uneven centro-symmetric solutions and thus prescribe $y(0) = y''(0) = 0$. As remaining necessary conditions, we specify the position of the first maximum: **(a)** $y'(0.5) = 0$, $y(0.5) = 0.205$; **(b)** $y'(0.5) = 0$, $y(0.5) = 0.2$; **(c)** $y'(0.3) = 0$, $y(0.3) = 0.16$; **(d)** $y'(0.5) = 0$, $y(0.5) = 0.1$.

(four in our case) for $y(x)$ and its derivatives needs to be provided. We concentrate on uneven centro-symmetric solutions, which directly prescribes two conditions: $y(0) = 0$ and $y''(0) = 0$. As was found before in a different context,[S11] the solution is extremely sensitive to the two remaining imposed conditions. For illustration, we depict four examples in Fig. S10. There, we provide slightly varying positions of the first maximum $[y'(x) = 0]$ as the remaining two necessary conditions. Numerical integration shows that little variations in these conditions lead to qualitatively different oscillatory solutions.[S15]

Altogether, we may conclude that the solutions resulting from Eq. (S18) sensitively depend on the input conditions. As noted above, we do not have access to the appropriate conditions applying at the significantly displaced end points of the embedded chain. The strategy that we resorted to is therefore to use as an input directly the shapes of the chains suggested by the experiments. We found good representations of the experimental observations using the polynomial form suggested by Eq. (5) in the main article. In particular, with regard to the pronounced displacements of the chain ends, this choice is preferred to, for instance, a sinusoidal ansatz. Then, instead of solving Eq. (S18) explicitly, we minimize the energy functional $E_{tot}[y(x)]$ with respect to the remaining degrees of freedom of the chain deformation (M, S, x_1 and x_2 in the main article). Thus, even if we have used an ansatz for the chain deformation, this remains a nonlinear approach as we evaluate the nonlinear contributions to the energy functional $E_{tot}[y(x)]$.

3.5 Oscillatory solutions in the linear regime

In the previous part, we have demonstrated that various complex solutions can result from the nonlinear nature of Eq. (S18). Here, we restrict ourselves to the situation in the inside of the magnetic chains for small amounts of deformation, i.e. at the onset of deformation. For this purpose, a linear stability analysis is performed by considering a linearized version of Eq. (S18). As a result, we obtain a condition describing the onset of

a linear deformational instability

$$W y''(x) + 2C_b y''''(x) + 2C_d y(x) = 0. \tag{S19}$$

This equation has solutions of the kind $y(x) \sim \exp(\pm iqx)$, with wavenumber

$$q^2 = \frac{W \pm \sqrt{W^2 - 16C_bC_d}}{4C_b}. \tag{S20}$$

The condition for the solutions to be purely oscillatory is $W^2/16C_bC_d > 1$ and defines an onset for this kind of deformation. It sets a threshold magnitude for the strength of the external magnetic field. Thus, for a perfectly oriented chain of identical particles in a spatially homogeneous elastic matrix, this linear stability analysis predicts a critical magnetic field amplitude above which an undulatory instability would arise in the inside of the chain. Our results are in agreement with the experimental observation of the wrinkles at onset in Fig. 1c and the final oscillatory shape in the inner part of the longer chains in Fig. 2a of the main article.

4 Technical description of the coarse-grained molecular dynamics simulations

4.1 Magnetic particles

In the molecular dynamics simulations, the centers of the magnetic particles and the nodes of the polymer mesh are treated as point particles in two-dimensional space. The magnetic particles additionally have one rotational degree of freedom, namely around the axis perpendicular to the model plane. As each magnetic particle is superparamagnetic, its magnetic moment is not affected by a rotation of the particle. Rather, the magnetic moment is determined by the magnetic field. Hence, we place the magnetic moment not on the rotating center of the particle, but rather on a separate virtual site which does not rotate. It is placed at the same location as the center of the magnetic particle. Virtual sites are particles, whose position is not determined by integrating an equation of motion, rather their position is calculated from the position and orientation of other particles. In this way, they allow us to introduce rigid extended bodies into a molecular dynamics simulation.[S16] Forces acting on any constituent of such a rigid body are transferred back to its center of mass, and thus included in the equation of motion of the rigid body.

Pairs of magnetic particles interact by the dipole-dipole interaction, Eq. (S6). The dipole moment of the particles is assumed to be determined entirely by the external magnetic field, and its magnitude is deduced from the experimental magnetization curve (Fig. S1b). This assumption is valid as long as the external field is much stronger than the field created by the other magnetic particles. In other cases, a self-consistent approach has to be used to determine the local magnetic fields. In addition to the dipole-dipole interaction, the magnetic particles interact via a truncated and shifted, purely repulsive Lennard-Jones potential mimicking a rigid-sphere interaction. We use the Weeks-Chandler-Andersen potential[S17] in the form

$$V_{WCA}\left(\frac{r}{\sigma}\right) = \begin{cases} 4\varepsilon\left[\left(\frac{r}{\sigma}\right)^{-12} - \left(\frac{r}{\sigma}\right)^{-6} + \frac{1}{4}\right] & \text{for } r \le r_c, \\ 0 & \text{otherwise,} \end{cases} \tag{S21}$$

where r is the distance between the particle centers, $\varepsilon = 1000$ denotes the energy scale of the potential, and $r_c = 2^{1/6}\sigma$ is the cut-off distance, for which we use the experimental diameter of 1.48 μm. The parameter σ denotes the root of the non-shifted potential and is used in the visualizations in Figs. 9 and 10.

4.2 Polymer mesh

The polymer matrix is modeled as a bead-spring network based on a hexagonal lattice. We use a lattice constant a of one third of the experimentally observed particle diameter, i.e., $a \approx 0.49$ μm. Along the initial chain direction, we use 601 mesh points, along the perpendicular direction 301. The mesh points on the boundary of the system are fixed, all other mesh points can move in the x- and y-directions. Adjacent mesh points interact via a non-linear elastic spring based on the FENE-potential.[S18] Here, we use a variant with

different cut-off values for compression and expansion. It is given by

$$\begin{aligned} V(r) &= -\tfrac{1}{2} K (r_0 - r_{\min})^2 \ln\left[1 - \left(\tfrac{r-r_0}{r_0 - r_{\min}}\right)^2\right] \quad \text{for } r < r_0, \\ V(r) &= -\tfrac{1}{2} K (r_{\max} - r_0)^2 \ln\left[1 - \left(\tfrac{r-r_0}{r_{\max} - r_0}\right)^2\right] \quad \text{for } r > r_0. \end{aligned} \tag{S22}$$

In these expressions, $K = 45$ controls the scale of the potential, the equilibrium distance $r_0 = a$ is equal to the lattice constant, while the minimum and maximum elongations, at which the potential diverges, are $r_{\min} = 0.1a$ and $r_{\max} = 3a$, respectively. The potential, as well as its second derivative, are continuous at the equilibrium extension $r = r_0$. In order to prevent any volume element from shrinking to zero, angular potentials are used on all pairs of neighboring springs attached to the same mesh site, encompassing an angle of 60° in the unstrained mesh. The potential has the same functional form as the distance-based potential in Eq. (S22), but with the values $K = 100$, $r_0 = \pi/3$, $r_{\min} = 0$, and $r_{\max} = \pi$. In the simulations both potentials are tabulated at 100 000 equally spaced intervals between the minimum and maximum extensions. Between those points, linear interpolation is used.

4.3 Particle-mesh coupling and boundary layer

The mesh spans the entire simulation area, including the area covered by the magnetic particles. In order to couple the polymer mesh to both, the translational and rotational motion of a magnetic particle, the seven mesh sites within the area of each magnetic particle are treated as virtual sites, rigidly following the motion of the magnetic particle. In other words, the mesh sites within the particle and the center of the magnetic particle form a rigid body. This additionally prevents a distortion of the gel matrix in the area occupied by the magnetic particles. Two variants of gel boundary layer around the particles are studied (Fig. 9 in the main article). In the case of a soft boundary layer, the mesh springs emerging from the mesh sites rigidly connected to the particle, are modeled as in Eq. (S22) with the same parameters as for the bulk. In the case of a stiff boundary layer, a potential is used which is stiffer by three orders of magnitude. The following parameters are used in this case: $K = 45\,000$, $r_{\min} = -2a$, and $r_{\max} = 4a$.

4.4 Equation of motion and integration

The simulations are performed in the canonical ensemble at a temperature of 300 K. All particles except for the virtual sites are propagated according to a Langevin equation. For any component in a Cartesian coordinate system, it is given by

$$m_p \dot{v}(t) = -\gamma v(t) + F + F_r, \tag{S23}$$

where m_p denotes the mass of the particle, v its velocity, F is the force due to the interaction with other particles, F_r denotes the random thermal noise, and γ is the friction coefficient. To maintain a temperature T, the thermal noise has to have a mean of zero and a variance of

$$\langle F_r^2 \rangle = 2 k_B T \gamma, \tag{S24}$$

where $k_B T$ denotes the thermal energy. For the rotational degree of freedom of each magnetic particle, the same equation of motion is used, but mass, velocity, and forces are replaced by moment of inertia, angular velocity, and torques, respectively. The friction coefficient, the thermal energy, and the mass of the mesh sites are all chosen to be unity, whereas the mass and rotational inertia of the centers of the magnetic particles are both 100. This slows down the relaxation time of the magnetic particles versus that of the polymer mesh and is helpful in stabilizing the simulation. The Langevin equation is integrated using a Velocity Verlet integrator. For the simulations with a stiff boundary layer, the time step is $dt = 0.001$, for a soft boundary layer it is $dt = 0.00004$. The simulations take approximately 100 000 time steps to converge.

References

[S1] F. Ziemann, J. Rädler and E. Sackmann, *Biophys. J.*, 1994, **66**, 2210–2216.

[S2] A. R. Bausch, W. Möller and E. Sackmann, *Biophys. J.*, 1999, **76**, 573–579.

[S3] P. Tordjeman, C. Fargette and P. H. Mutin, *J. Rheol.*, 2001, **45**, 995–1006.

[S4] T. G. Mason, T. Gisler, K. Kroy, E. Frey and D. A. Weitz, *J. Rheol.*, 2000, **44**, 917–928.

[S5] http://www.physics.emory.edu/faculty/weeks//idl/index.html.

[S6] T. G. Mason and D. Weitz, *Phys. Rev. Lett.*, 1995, **74**, 1250–1253.

[S7] H. Raich and P. Blümler, *Concept. Magn. Reson. B*, 2004, **23B**, 16–25.

[S8] C. Goubault, P. Jop, M. Fermigier, J. Baudry, E. Bertrand and J. Bibette, *Phys. Rev. Lett.*, 2003, **91**, 260802.

[S9] L. Landau and E. Lifshitz, *Elasticity theory*, Pergamon Press, 1975.

[S10] I. Gelfand and S. Fomin, *Calculus of variations*, Prentice-Hall Inc., Englewood Cliffs, NJ, 1963.

[S11] G. W. Hunt, M. Wadee and N. Shiacolas, *J. Appl. Mech.*, 1993, **60**, 1033–1038.

[S12] B. Audoly, *Phys. Rev. E*, 2011, **84**, 011605.

[S13] H. Diamant and T. A. Witten, *arXiv preprint arXiv:1009.2487*, 2010.

[S14] H. Diamant and T. A. Witten, *Phys. Rev. Lett.*, 2011, **107**, 164302.

[S15] Wolfram Research, *Mathematica 10.0*, 2014.

[S16] A. Arnold, O. Lenz, S. Kesselheim, R. Weeber, F. Fahrenberger, D. Röhm, P. Košovan and C. Holm, *Meshfree Methods for Partial Differential Equations VI*, 2013, pp. 1–23.

[S17] J. D. Weeks, D. Chandler and H. C. Andersen, *J. Chem. Phys.*, 1971, **54**, 5237–5247.

[S18] H. R. Warner Jr., *Ind. Eng. Chem. Fundam.*, 1972, **11**, 379–387.